Open-loop shape control for continuous microelectromechanical system deformable mirror

Alioune Diouf,[1,*] Andrew P. Legendre,[1] Jason B. Stewart,[2] Thomas G. Bifano,[1,2] and Yang Lu[1]

[1]Photonics Center, Boston University, 15 Saint Mary's Street, Boston, Massachusetts 02215, USA

[2]Boston Micromachines Corporation, 36 Spinelli Drive, Cambridge, Massachusetts 02138, USA

*Corresponding author: alioune@bu.edu

Received 2 April 2010; revised 15 August 2010; accepted 16 August 2010; posted 17 August 2010 (Doc. ID 126445); published 10 September 2010

We characterize the errors associated with open-loop control of a microelectromechanical system deformable mirror (DM) using an approach that combines sparse calibration of the electrostatic actuator state space with an elastic plate model of the mirror facesheet. We quantify sources of measurement error and modeling error and demonstrate that the DM can be shaped in a single step to a tolerance of ~8 nm of that achievable with iterative feedback-based closed-loop control. Zernike polynomials with up to 2.5 μm amplitude were made with this approach and yielded a shape error of <25 nm rms in most cases. Residual errors were shown to be due primarily to spatial resolution limits inherent in the DM (e.g., uncontrollable errors). © 2010 Optical Society of America

OCIS codes: 230.4040, 230.3990.

1. Introduction

Accurate open-loop control of deformable mirrors (DMs) promises to enable an emerging class of adaptive optics imaging instruments, those in which conventional feedback from a wavefront sensor is not practical. Several such advanced instruments are envisioned for next-generation telescopes and microscopes. For example, multiobject adaptive optics is an instrument concept that would allow high-resolution imaging of a large number of faint objects across a wide field of view in an extremely large telescope. This concept would require controlling multiple DMs in an open loop because the DMs would modify the wavefront *downstream* of the wavefront sensor [1–3]. In microscopy, open-loop DM control has enabled new control approaches to nonlinear microscopy for high-resolution subsurface imaging. In two-photon excitation fluorescence imaging through biological tissue, for example, it has been found that even without a wavefront sensor for feedback, precise open-loop control of DM shapes in an adaptive optics system can yield rapid compensation of low-order aberrations [4–7].

The development of an accurate open-loop control algorithm of the microelectromechanical system (MEMS) DM with a continuous facesheet (Fig. 1) is complicated by the nonlinear relationship between the input voltage and the resulting actuator deflection as well as the effect of the coupling between neighboring actuators [8]. Previous open-loop control algorithms for these DMs used empirical and mathematical models [8–10]. Morzinski *et al.* [10] were able to predict voltages for 500 nm amplitude mirror shapes with residual errors of 15 nm rms using an empirical calibration of actuator behavior. Vogel and Yang [9] introduced a fully analytical approach using a coupled system of nonlinear partial differential equations (PDEs) for the mirror facesheet and actuator. Later, Stewart *et al.* [11] used an approach similar to the Morzinski method with a different

0003-6935/10/31G148-07$15.00/0
© 2010 Optical Society of America

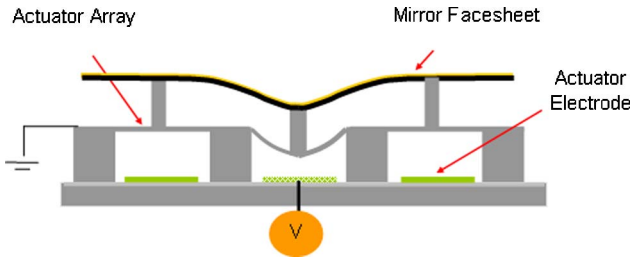

Fig. 1. (Color online) Continuous facesheet MEMS DM cross section.

calibration scheme and a different approach of treating the plate equation of the mirror facesheet and were able to predict voltages for 1.5 μm amplitude mirror shapes with residual errors of 15 nm rms.

Prior proof-of-concept studies of open-loop control with the DMs used in the present work (Boston Micromachines Multi-DM 140-actuator continuous) were sometimes limited in scope. For example, open-loop control algorithms were sometimes evaluated, using as a target shape a previously measured surface map of the actuated DM. Also, these prior studies often tested the controller against relatively small peak-to-valley deflections (less than 600 nm), though these DMs have a usable range of up to 3.5 μm. Using a previously measured DM mirror shape ensures that the desired control target shape is achievable but fails to test the effectiveness of control for more arbitrary wavefront shapes, which might be comprised of spatial frequencies that exceed those within the DM controllable range. Another limitation in the prior work was that open-loop control algorithms for MEMS DMs were assessed by measuring the change in shape of the DM with respect to its initial, unpowered shape. In the current work, we report on efforts to produce a prescribed net shape, including compensation of any unpowered shape error on the DM. The former approach will be referred to in this paper as "differential" shape control, while the latter will be referred to as "nondifferential" or "true" shape control. In our prior efforts to develop an open-loop control algorithm [8], we postulated that the single-actuator empirical calibration employed might be improved by calibration of all actuators in the array to account for any actuator variability within the array. In the work reported here, we demonstrate results from a sparse, fast, parallel calibration of all actuators to account for small systematic differences among actuators in the array. We compare errors associated with open-loop control using a single-actuator calibration to that achieved with full array calibration. Another minor improvement made to the open-loop control algorithm was an enhancement to the filtering method used in calibration experiments. These improvements have led to increased accuracy over a wider variety of deflection profiles, including flattening the mirror, and controlling "nondifferential" shapes of mathematically defined ideal shapes such as low-order Zernike polynomials. We begin with a review of the different open-loop control algorithms for MEMS DMs, followed by a derivation of the form of the facesheet plate equation. A demonstration of the algorithm for large amplitude (>1.5 μm) and small amplitude (500 nm) deflections follows along with a quantification of the sources of errors.

2. Deformable Mirror Model for Open-Loop Control

A 400 μm pitch DM with 3.5 μm stroke and 144 actuators (12 × 12) is used to demonstrate the open-loop control and evaluate algorithm and system errors. The DM has an aperture width of 4.4 mm and a facesheet thickness of 3 μm. One of the characteristics of the continuous facesheet DM is interactuator coupling through the mirror facesheet [10–12]. Overcoming interactuator mechanical coupling through the mirror facesheet is achieved by establishing a DM model that consists of two coupled mechanical subsystems: the continuous facesheet and the array of actuators connected to the facesheet via rigid posts [8–10]. We begin our mirror facesheet model with the generalized form of out-of-plane plate deflections experiencing bending and stretching and show the assumptions and derivations of the in-plane forces used in Stewart *et al.* [11]. We model the out-of-plane deflections using a fourth-order PDE with a nonlinear second-order term to account for the effects of the facesheet stretching [13]:

$$\nabla^4 w(x,y) = \frac{1}{D}\left(q(x,y) + N_x \frac{\partial^2 w(x,y)}{\partial x^2} + N_y \frac{\partial^2 w(x,y)}{\partial y^2} + 2N_{xy}\frac{\partial^2 w(x,y)}{\partial x \partial y}\right), \quad (1)$$

where N_x and N_y are in-plane membrane forces per unit length (due to stretching). N_{xy}, the in-plane shear force per unit length, is ignored in this problem because the mirror facesheet is rigidly attached to actuators via posts experiencing no bending moments; $q(x,y)$ is the surface normal distributed load responsible for producing mirror facesheet deflection $w(x,y)$, and D is the plate flexural rigidity, given by

$$D = \frac{Eh^3}{12(1-\nu^2)}, \quad (2)$$

where E is the Young modulus, ν is the Poisson ration, and h is the facesheet thickness. The expressions for the in-plane membrane forces N_x that arises due stretching can be obtained from the stress resultant σ_{xx}:

$$N_x = \int_h \sigma_{xx} \mathrm{d}z = \int_h \frac{E}{1-\nu^2}\varepsilon_x \mathrm{d}z. \quad (3)$$

The strain can be approximated as $\frac{1}{2}(\frac{\partial w}{\partial x})^2$, and (3) becomes

$$N_x = \frac{Eh}{2(1-\nu^2)}\left(\frac{\partial w}{\partial x}\right)^2. \quad (4)$$

Inserting Eq. (4) and an analogous expression for N_y into Eq. (1), we obtain the governing equation for out-of-plane deflections of a linear elastic plate experiencing bending and stretching as presented in [8]:

$$\nabla^4 w(x,y) = \frac{q(x,y)}{D} + \frac{6}{h^2}\left(\frac{\partial^2 w(x,y)}{\partial x^2}\left(\frac{\partial w(x,y)}{\partial x}\right)^2 + \frac{\partial^2 w(x,y)}{\partial y^2}\left(\frac{\partial w(x,y)}{\partial y}\right)^2\right). \quad (5)$$

The assumptions and limitations of this model are stated in Stewart *et al.* [11] and are not repeated here. We use the numerical approximation of the biharmonic and Laplacian (fourth- and second-order derivatives) to compute the mirror forces for given mirror deflections. The remaining forces (actuator and electrostatic) are not calculated. Instead, our algorithm proceeds with an empirical characterization of the DM actuators, which consists of applying a variety of arbitrary shapes of known voltages to create a voltage lookup that spans the achievable mirror shape space. The main drawback of this technique is its susceptibility to noise because of the four numerical differentiations to approximate the biharmonic.

3. Other Microelectromechanical System Deformable Mirror Open-Loop Control Approaches

Modeling efforts carried out by Morzinski *et al.* [10] used a similar model to the one presented in this paper without a nonlinear second-order term to account for the effects of facesheet stretching at large deflections (>1.5 μm). Their routine was able to predict voltages for 500 nm amplitude mirror shapes with residual errors of 15 nm rms. Their approach for solving for forces significantly differs from the one we proposed in Stewart *et al.* [11]. The authors considered an influence function $K(x,y,x_n,y_n)$ giving deflection (x,y) when a unit load is applied at some point (x_n,y_n). Following a circular plate approximation of the rectangular plate equation, a free-space Green function is utilized for the biharmonic operator.

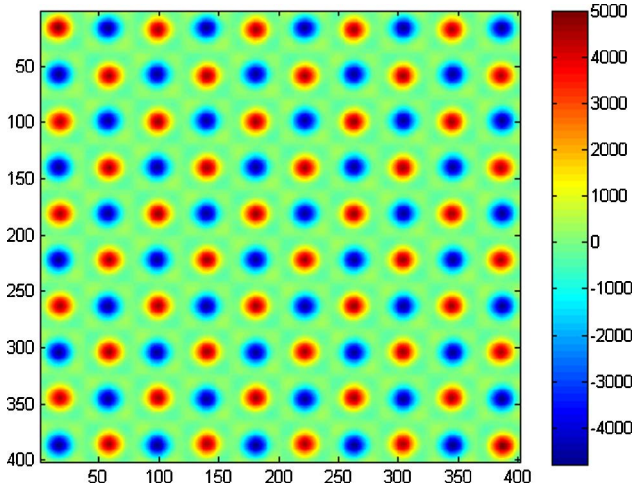

Fig. 2. (Color online) Butterworth filtered DM pressure from "checkerboard" pattern shape with cutoff frequency = 250 μm.

Vogel and Yang [9] introduced a coupled system of nonlinear PDEs for the mirror facesheet and actuator. This model did not take into account nonlinearity when the displacements are large relative to the plate thickness (stretching) and assumed a parallel plate electrostatic deflection of the actuators. Vogel *et al.* recently presented a parameter estimation method based on their prior work. In this work, the facesheet stretching is accounted for with the inclusion of a linear second-order tension term and the actuators are treated like linear springs [14]. The model also includes actuator offset terms to account for slight initial dome shapes exhibited by many MEMS DMs: $D_{\mathrm{fs}}\nabla^4 w - T\nabla^2 w = \sum_{i=1}^{n_a} p_i \delta(x - x_i)$, where $w(\mathbf{x})$ is the out-of-plane deflection of the facesheet at location $\mathbf{x} = (x,y)$, D_{fs} is the flexural rigidity of the facesheet, T is the facesheet tension, p_i is the point load of the facesheet due to the ith actuator, $\mathbf{x}_i$ is the actuator location, $\delta(\cdot)$ is the Dirac-delta, n_a is the number of actuators, and ∇^4 is the squared Laplacian operator. The algebraic form of the actuator deflection is assumed to have the form $z_i = r(p_i, V_i)$, $i = 1, \ldots, n_a$, where z_i is the deflection of the ith actuator and V_i is the associated voltage to cause the deflection. Applying to all actuators a bias voltage $\bar{V}$ yielding zero deflection ($p_i = 0$ when bias $= \bar{V}$), followed by a voltage V_i resulting in very small deflection, it can be shown that the facesheet deflection of the facesheet DM caused by the net voltage change $a_i = V_i - \bar{V}$ is $w(x_i) = \frac{\partial r(0,\bar{V})}{\partial p} p_i + \frac{\partial r(0,\bar{V})}{\partial V} a_i + E({p_i}^2) + E({a_i}^2)$, where E is an error function. The authors then consider the case of small deflection regime with a linear actuator response of the form: $r(p,V) = k^{-1}p + \gamma V$. Ignoring the error terms and solving for p_i, the DM PDE with a linear actuator response function proposed by Vogel *et al.* [14] takes the form $\nabla^4 w + \beta_1 \nabla^2 w + \beta_2 \sum_{i=1}^{n_a} w(x_i)\delta(x - x_i) = \beta_3 \sum_{i=1}^{n_a} a_i \delta(x - x_i)$; where $\beta_1 = \frac{T}{D_{\mathrm{fs}}}$, $\beta_2 = \frac{k}{D_{\mathrm{fs}}}$, $\beta_3 = \gamma\beta_2$.

A significant departure from their previous algorithm involves the use of *output least squares* to estimate parameters. Using this method, the parameters of the PDE (β parameters) are determined by minimizing the deviation between the output of the model and the observation data through an *objective* or *cost function*. The algorithm thus searches for parameter values that yield a model that provides optimal fit of the data. This approach is robust, as it involves no numerical differentiation, in contrast to our approach in which fourth-order numerical differentiation amplifies high spatial frequency noise in the calibration measurement. However, MEMS DMs actuator nonlinear effects and their interactions are not yet well understood, and as a result, modeling of the actuator response for large deflections has not yet been achieved.

4. Actuator Calibration and Open-Loop Control Scheme

The major refinements to our previous algorithm relate to measurement filtering (Fig. 2), characterization methods (Fig. 3), and controlling the nondifferential shape of the mirror. These changes have led to increased accuracy over a wider variety of deflection profiles.

As in [8], the open-loop control software is based in MATLAB, which also performs all hardware communication and data analysis. The software controls a 14 bit high-voltage power supply, and a Zygo NewView 6000 surface mapping interferometric microscope is used to asynchronously apply the desired shapes to the DM and record surface data. The driver voltage resolution is ~20 mV. The microscope magnification and CCD resolution used to view the full DM aperture determine the number of surface data points used in mirror calibration, which is about 40 pixels per subaperture.

Filtering the deflection measurement during calibration is an essential step to reduce the effect of measurement noise and mirror surface defects on the fourth-order differentiation that yields mirror forces. Previous work on control of continuous MEMS DMs has been conducted with filter settings that block spatial frequency range of the mirror [8]. Using that filter led to unacceptable loss of information regarding the bending and stretching of the DM. In this work we found that a better filter to employ was a fourth-order Butterworth with a cutoff wavelength (250 μm) just below two cycles per actuator spacing. A Butterworth filter is maximally flat in the passband, so that no deflection information is lost. It exhibits a gradual roll-off above the cutoff frequency. The filtering method was effective because of the relatively small DM surface defects and the low spatial frequency content of the measurement noise. The effectiveness of the filter can also be attributed to the bending and stretching of the DM having either relatively low spatial frequency effects, or it is only the low spatial frequency components of these effects that contributed to the model. The rms error between the filtered and unfiltered data is 2 nm. After low-pass filtering, the calculated forces are largest in the vicinity of the posts, where they would be expected for this physical system. Another source of error is the nonuniformity of actuator mechanical behavior that results from tolerances in the MEMS manufacturing process. The error introduced by calibrating a single actuator (and assuming all others to be identical) as opposed to calibrating all actuators was found to be 14 nm rms. In open-loop control, this led to DM flattening results with 13–15 nm rms error for the single-actuator calibration as opposed to 6 nm rms for the full array actuator calibration (Fig. 4). Similarly, the residual error

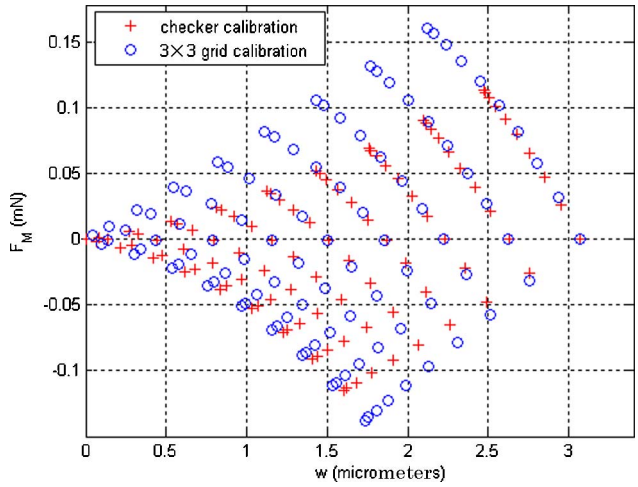

Fig. 3. (Color online) Slice of the dataset $\{w, F_M, V\}$ shown for actuator 66. Mirror forces (F_M) plotted against deflections $w(x,y)$. In the "checker" pattern (red +), actuators are divided in two groups and a range of linearly spaced square voltages is applied to each group independently. The "3 × 3 grid" is essentially a single-actuator calibration where a group of nine actuators are considered at a time; identical voltages are applied to a ring (the outer eight) to vary F_M at the central actuator.

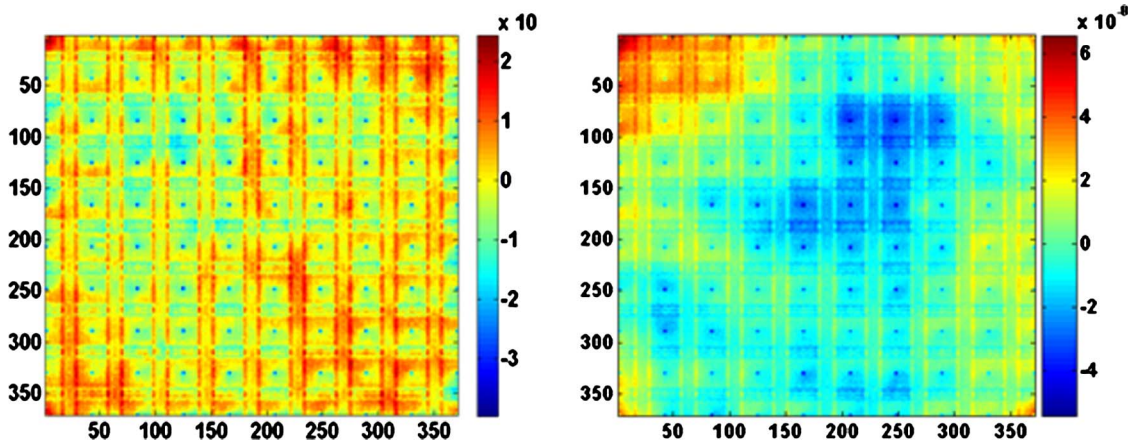

Fig. 4. (Color online) Open-loop DM flattening. The DM is flattened to 6 nm within the unfiltered rms error using the calibration map from all actuators (left). This surface figure is dominated by high spatial frequency DM features that are not within the controllable band. Typical surface figure rms flattening using single-actuator calibration (right). With single-actuator calibration, some lower order shape errors within the controllable band remain uncorrected.

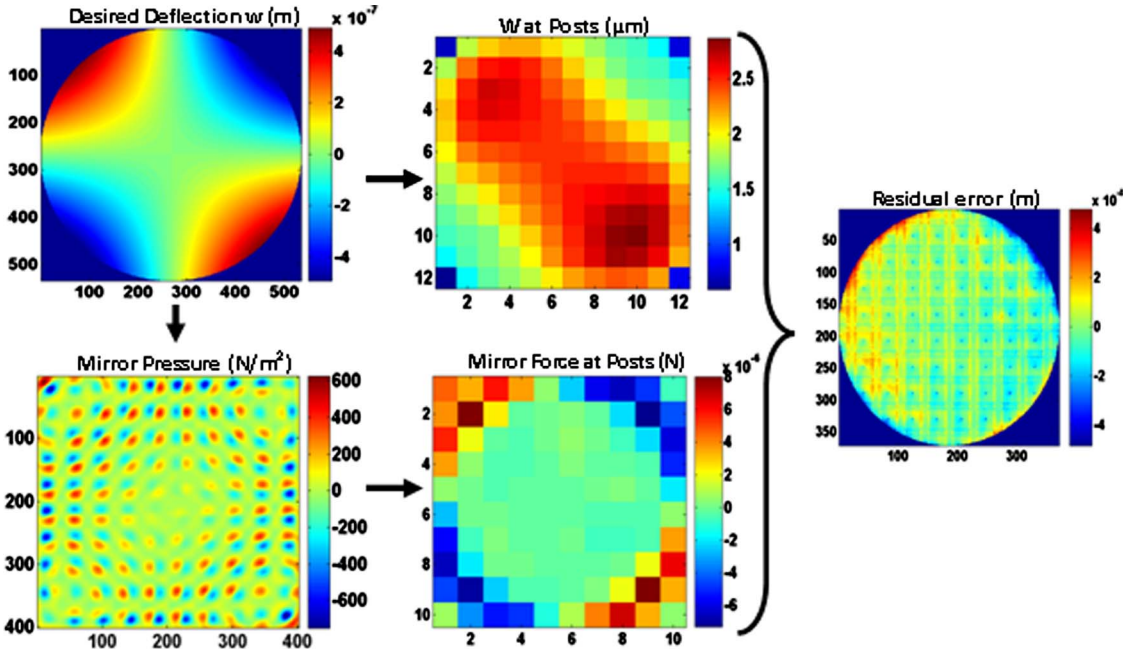

Fig. 5. (Color online) Demonstration of open-loop control for ideal 1 μm peak-to-valley astigmatism Zernike. The difference between the desired and achieved shape, the residual error (far right) is less than 9 nm rms, just 3 nm above the minimum achievable error (6 nm rms).

from an open-loop shape control of Zernike shapes was found to be ~10 nm rms smaller for the full actuator calibration. To account for actuator nonuniformity, a calibration table was created for each individual actuator. Two methods for fast calibration of all actuators have been explored. We designate these as the *checker* and *grid* patterns. Both of these calibration methods are fully scalable, requiring the same number of measurements to characterize a 3 × 3 actuator array as they would for any larger square array (including 12 × 12). For the checker calibration, the actuators are divided into two groups in a *checkerboard* pattern. A range of voltages at regular steps is applied to each group independently, and information is recorded in parallel for all actuators with each interferometric surface measurement. The benefit of this method is that it can be completed in the same amount of time as a single-actuator calibration. As can be observed in Fig. 3, the checkerboard pattern is not amenable to high forces (compared to the grid calibration discussed below); therefore, the checker method does not adequately characterize the high-force mirror states.

The grid calibration places each 3 × 3 array of actuators into a calibration group. Each of the nine actuators in the group is calibrated independently, but all 3 × 3 groups are processed in parallel. This method characterizes the full range of possible mirror states, but requires nine times as much calibration time to complete as a single-actuator calibration or checker calibration. This longer calibration time could lead to inaccurate results if the measurement setup is susceptible to drift, which was measured to be 2 nm rms over 8 *h*. The difference in rms shape error associated with using the checker calibration method as opposed to grid calibration when controlling shapes known to have mirror forces not spanned by the checker map varied from 10 to 30 nm rms.

For each actuator, 20 data triples (applied voltage V, mirror force F, and mirror deflection w) are measured and interpolated to create an actuator lookup table. It was verified that the interpolation yields zero residuals at the measured sets. Direct measurement of interpolated data triples obtained by changing the measured sets showed that the interpolation error can result in up to 5 nm rms error.

Table 1. Root Mean Square Error of Zernike Shapes Tested

Shape	Peak-to-Valley Deflection (μm)	Residual Error (nm rms)	
		Open Loop	Closed Loop
Astigmatism	0.5	8	8
	1	9	9
	1.5	12	11
	2	19	14
	2.5	24	19
Focus	0.5	12	10
	1	18	15
	1.5	25	21
	2	30	28
	2.5	41	36
Trefoil	0.5	15	8
	1	18	9
	1.5	23	12
	2	28	16
	2.5	36	24
Coma	0.5	12	12
	1	19	18
	1.5	29	25
	2	40	33
	2.5	90	38

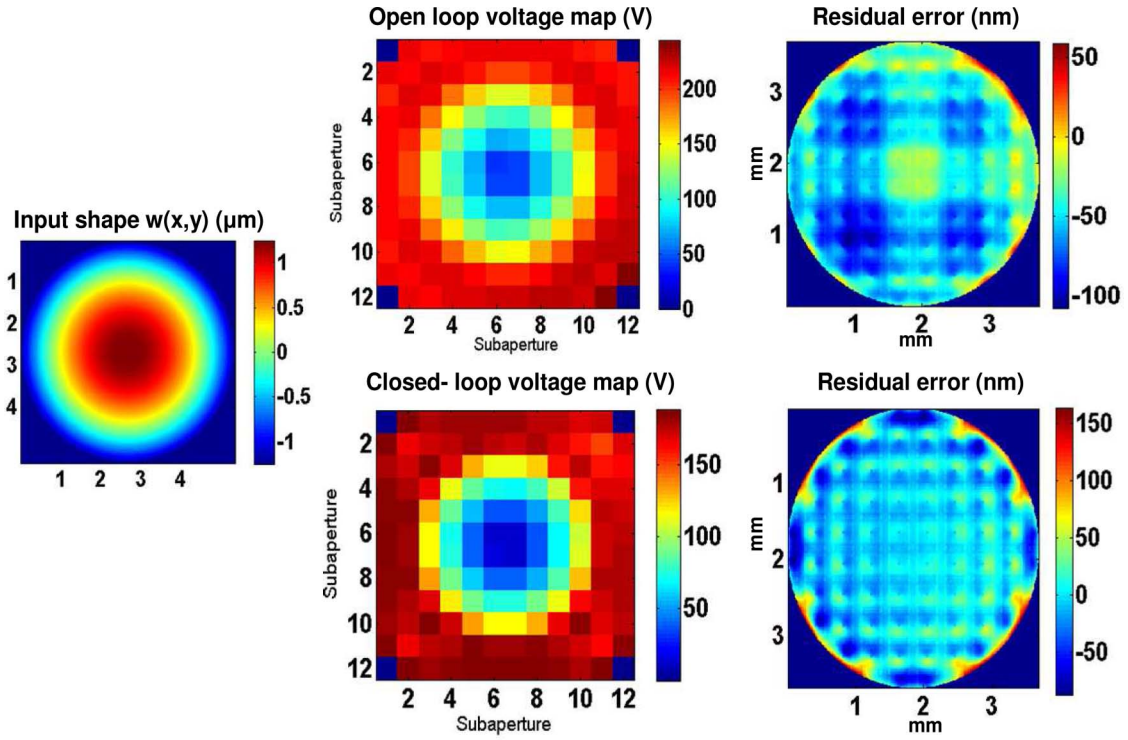

Fig. 6. (Color online) Comparison between open-loop and closed-loop performance for ideal focus Zernike shape. Input 2 μm peak-to-valley focus shape (left). Voltage prediction (middle) using developed open-loop control algorithm (top) and closed-loop algorithm (bottom). Residual errors between input and achieved shape using open-loop (30 nm rms) (top right). The equivalent closed-loop residual error (bottom right) is 28 nm rms.

The initial (unpowered) shape of the mirror was added to the calibration deflection (w) to allow control to the desired net shape. This measurement was filtered with a cutoff frequency of a half pitch per actuator to ensure adequate rejection of differentiation errors. In an initial test of the refined open-loop control algorithm, the DM was flattened to 6 nm rms in a single step after calibration.

5. Algorithm Evaluation and Discussion

The demonstration of this open-loop DM control algorithm was performed using ideal, mathematically defined target shapes. This is a departure from our earlier open-loop control evaluation where the target shapes were first measured on the DM. The first shape used in this demonstration is a Zernike astigmatism of 1 μm peak-to-valley deflection applied directly to the MEMS DM. The resulting residual wavefront shape error from our algorithm is ~9 nm rms error for this target shape (Fig. 5).

The subsequent open-loop demonstration exercises consisted of evaluating shapes that push the limit of the DM achievable spatial frequencies. This is accomplished with higher order Zernike polynomials at higher deflections (1.5 μm and 2.5 μm peak to valley). For the 1.5 μm peak-to-valley deflections, the residual shape errors after the open-loop ranged from 12 nm rms for lower order Zernike shapes, such as astigmatism, to 29 nm rms for coma. Similarly, the residual shape error for a 2.5 μm deflection astigmatism and coma were 19 and 40 nm rms, respectively. Table 1 lists the complete set of shapes evaluated with corresponding residual shape errors after the open loop.

Finally the open-loop control algorithm performance is compared to that of its closed-loop counterpart, and shapes with peak-to-valley deflections using the maximum achievable stroke of the tested device (3.5 μm) are tested. A closed-loop control algorithm routine that used measured Zygo interferometric surface map data as feedback was implemented using the same target shapes tested with the open-loop control algorithm. Overall, the open-loop control algorithm performed close to that of the closed-loop control algorithm. For higher amplitude shapes (peak-to-valley above 2 μm) and higher order Zernike shapes (trefoil), the closed-loop control outperforms the open-loop algorithm (Fig. 6). The difference in residual shape errors between open- and closed-loop control algorithms are attributable to the limitations of the calibration methodology employed. For example, the 3×3 block pattern calibration stroke limitation can be seen in the apparent "blocky" pattern of the open-loop residual errors.

6. Conclusion

The error associated with open-loop control with a single-actuator calibration as opposed to a lookup table for each individual actuator was found to be 14 nm rms. The grid calibration method was found to be the most accurate calibration method, but it is performed over 8 h introducing 2 nm rms errors from drift. The empirical grid calibration produces datasets that span the entire range of voltage,

deflection, and force triples possible. The fitting error of a calibration dataset is 5 nm rms. The checker calibration method makes the same number of measurement as in a single-actuator calibration, but does not span the entire space of deflection, voltage, and force triples. The error introduced using a checker calibration instead of the grid calibration is 10 to 30 nm rms for shapes with forces not in the checker space. Taking all these errors into consideration, the open-loop control algorithm was amenable to control the DM surface in a single iteration, based on a sparse actuator calibration and computationally efficient algorithm. The nonuniformities from the initial shape of the mirror were added by including the 0 V mirror shape in every desired mirror deflection $w(x,y)$. The mirror is then flattened to 6 nm rms, representing the effective zero-deflection plane. This ensures that the mirror forces from the analytical model of the DM truly represent forces resulting from facesheet deflections. Evaluation was then conducted for higher order Zernike shapes and a larger stroke than previously demonstrated in [8–10]. Although this work was performed on a 12×12 DM, the behavior of devices with higher actuator count is not expected to reduce control accuracy.

References

1. S. M. Ammons, E. A. Laag, R. Kupke, D. T. Gavel, and C. E. Max, "Enabling laboratory demonstrations of multi-object adaptive optics with linearity calibrations," Proc. SPIE **6691**, 669108 (2007).
2. F. Assémat, E. Gendron, and F. Hammer, "The FALCON concept: multi-object adaptive optics and atmospheric tomography for integral field spectroscopy—principles and performance on an 8-m telescope," Mon. Not. R. Astron. Soc. **376**, 287–312 (2007).
3. E. A. Laag, S. M. Ammons, D. T. Gavel, and R. Kupke, "Multi-conjugate adaptive optics results from the laboratory for adaptive optics MCAO/MOAO testbed," J. Opt. Soc. Am. A **25**, 2114–2121 (2008).
4. M. J. Booth, M. A. Neil, R. Juskaitis, and T. Wilson, "Adaptive aberration correction in a confocal microscope," Proc. Natl. Acad. Sci. USA **99**, 5788–5792 (2002).
5. M. A. A. Neil, R. Juskaitis, M. J. Booth, T. Wilson, T. Tanaka, and S. Kawata, "Adaptive aberration correction in a two-photon microscope," J. Microsc. **200**, 105–108 (2000).
6. D. Debarre, M. J. Booth, and T. Wilson, "Image based adaptive optics through optimisation of low spatial frequencies," Opt. Express **15**, 8176–8190 (2007).
7. Y. Zhou, T. G. Bifano, and C. Lin, "Adaptive optics two-photon fluorescence microscopy," Proc. SPIE **6467**, 646705 (2007).
8. J. B. Stewart, A. Diouf, Y. Zhou, and T. G. Bifano, "Open-loop control of a MEMS deformable mirror for large-amplitude wavefront control," J. Opt. Soc. Am. A **24**, 3827–3833 (2007).
9. C. R. Vogel and Q. Yang, "Modeling, simulation, and open-loop control of a continuous facesheet MEMS deformable mirror," J. Opt. Soc. Am. A **23**, 1074–1081 (2006).
10. K. M. Morzinski, K. B. Harpsoe, D. T. Gavel, and S. M. Ammons, "The open-loop control of MEMS: modeling and experimental results," Proc. SPIE **6467**, 64470G (2007).
11. J. B. Stewart, T. G. Bifano, S. A. Cornelissen, P. Bierden, M. Levine, and T. Cook, "Design and development of a 331-segment tip-tilt-piston mirror array for space-based adaptive optics," Sens. Actuators A, Phys. **138**, 230–238 (2007).
12. T. G. Bifano, R. K. Mali, R. K. Dorton, J. Perreault, N. Vandelli, M. Horenstein, and D. A. Castanon, "Continuous-membrane surface-micromachined silicon deformable mirror," Opt. Eng. **36**, 1354–1360 (1997).
13. S. Timoshenko and S. Woinowsky-Krieger, *Theory of Plates and Shells* (McGraw-Hill, 1976).
14. C. R. Vogel, G. Tyler, R. Conan, and C. Blain, "Fast, robust parameter estimation and open-loop control of point-actuated, continuous-facesheet deformable mirrors," in *Adaptive Optics: Methods, Analysis and Applications*, OSA Technical Digest (CD) (Optical Society of America, 2009), paper AOThD4.